Chapter 5

Stress-strain curves

5.1 Introduction

Now we want to look into the stress-strain response for different loading conditions and grain geometries. Stress-strain curves are a standard result of fatigue experiments. We, therefore, have to find a a strain measure for the stress-controlled simulations we performed so far. For the strain-controlled simulations we have to setup a method to prescribe displacements.

Until now, the traction-free boundary conditions on the simulated grain were taken into account analytically. This approach is applicable when modeling dislocations in half-space with a uniform applied stress, as it was mentioned in chapter 2. For strain-controlled simulations, as well as for those with more complex boundary conditions it is not feasible to include the boundary conditions analytically and a more general approach to the boundary value problem is necessary. We use the superposition method proposed by Van der Giessen and Needleman [28] here.

The approach proposed originally by Van der Giessen and Needleman uses the elastic solution of a dislocation in infinite space. Here, as in [2] we use the half-space solution because it satisfies the boundary conditions at the free surface intrinsically and therefore reduces the numerical effort of the boundary problem significantly. However, both approaches, i.e. the infinite space and the half-space solution, give the same result since the solution to an elastic boundary value problem is unique.

The formulation adopted here is one for small strains and does not take the surface steps into account that are produced by dislocations moving out at the free surface. In chapter 4 an approximate approach to include the effects of surface roughness is suggested. Deshpande et al. [49] have proposed a finite strain formulation of the superposition method. In the finite strain model, re-meshing is necessary to account for the change in geometry. Moreover, the elements at the surface step would have to be small enough to capture the

surface roughness, which is on the order of a nanometer. On the other hand, the mesh has to cover the grain, which is on the order of a micrometer. Therefore, a complex remeshing routine is necessary to prevent very elongated elements and a very large number of elements is needed. This would lead to a significant increase in the computational costs, which are already substantial in the small-strain formulation. Therefore, we use the small-strain formulation here.

5.2 Model for strain-controlled simulations

The small-strain framework of Van der Giessen and Needleman [28] is used here to solve quasi-static boundary value problems for bodies with dislocations. As a reminder, at some instant the body contains a distribution of dislocations which are regarded as point defects in this two-dimensional representation and are embedded in a linear elastic isotropic continuum. At the boundary $S = S_u \cup S_f$ mixed boundary conditions are prescribed; displacement boundary conditions are prescribed along S_u while tractions are prescribed along the S_f boundary. The tractions on the boundary are $\boldsymbol{T} = \boldsymbol{n}\boldsymbol{\sigma}$, where $\boldsymbol{n}$ is the outer normal to the boundary.

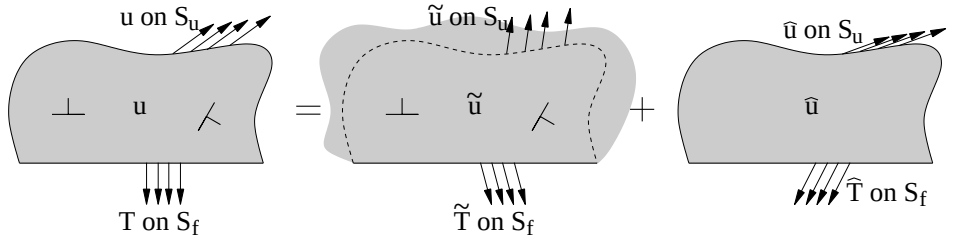

Figure 5.1: The boundary value problem as superposition of a discrete dislocation problem for a half-space and a correction for the boundary conditions.

The elastic fields of the body containing the dislocations are calculated, as shown in Figure 5.1, by superposition of the elastic fields of the dislocation distribution $\tilde{}$ and the $\hat{}$ fields, which correct the boundary conditions:

$$\begin{aligned} \boldsymbol{\sigma} &= \tilde{\boldsymbol{\sigma}} + \hat{\boldsymbol{\sigma}} \\ \boldsymbol{u} &= \tilde{\boldsymbol{u}} + \hat{\boldsymbol{u}} \\ \boldsymbol{\varepsilon} &= \tilde{\boldsymbol{\varepsilon}} + \hat{\boldsymbol{\varepsilon}} \end{aligned}$$

Here, the elastic fields of the dislocation distribution $\tilde{}$ are calculated as the sum of the elastic fields of the individual dislocations I:

$$\tilde{\boldsymbol{\sigma}} = \sum_I \tilde{\boldsymbol{\sigma}}^I$$
$$\tilde{\boldsymbol{u}} = \sum_I \tilde{\boldsymbol{u}}^I$$
$$\tilde{\boldsymbol{\varepsilon}} = \sum_I \tilde{\boldsymbol{\varepsilon}}^I$$

These elastic fields are evaluated using Freund's [30] equations, mentioned in chapter 2 and which already satisfy the free surface boundary conditions. The boundary conditions on the other boundaries have to be accounted for through the $\hat{}$ correction fields.

The $\tilde{}$ fields are continuous and non-singular at any point except at the sites of the dislocations. Therefore, the $\hat{}$ fields are also continuous and non-singular along the boundary and can be easily solved by numerical techniques such as the finite element method, which is used here. Therefore, the governing equations for the $\hat{}$ fields read (cf. chapter 1)

$$\begin{aligned} \mathrm{div}\hat{\boldsymbol{\sigma}} &= \mathbf{0}; \\ \hat{\boldsymbol{\varepsilon}} &= \frac{1}{2}\left(\mathrm{grad}\,\hat{\boldsymbol{u}} + \mathrm{grad}^{\mathrm{T}}\hat{\boldsymbol{u}}\right); \\ \hat{\boldsymbol{\sigma}} &= \boldsymbol{C}\hat{\boldsymbol{\varepsilon}}, \end{aligned}$$

which have to be satisfied throughout the body. The boundary conditions for the $\hat{}$ fields are

$$\begin{aligned} \boldsymbol{n}\hat{\boldsymbol{\sigma}} = \hat{\boldsymbol{T}} = \boldsymbol{T} - \tilde{\boldsymbol{T}} \quad \text{on} \quad S_f \\ \hat{\boldsymbol{u}} = \boldsymbol{u} - \tilde{\boldsymbol{u}} \quad \text{on} \quad S_u \end{aligned}$$

The iterative method of the simulation is as follows. First, the updated dislocation distribution is calculated based on the singular long-range dislocation interaction forces, the free surface image stress and the correction fields from the previous time step. To that end, the applied stress in equation (2.3) already indicated with a $\hat{}$ is replaced by the correction stress and the dislocations move according to the drag relation (2.4). Then, the surface tractions and displacements due to this dislocation distribution are evaluated. After that, the boundary conditions for the finite element method are calculated as $\hat{\boldsymbol{T}} = \boldsymbol{T} - \tilde{\boldsymbol{T}}$ to fulfill the prescribed boundary conditions. After solving for $\hat{\boldsymbol{\sigma}}$ the next time step is started.

Here, we use the constitutive rules of the 2DD model, as described in chapter 2. The extended rules of the 2.5DD model are not used because they are computationally very expensive. The 2.5DD model is barely feasible for the stress-controlled simulation, as shown in chapter 2; since solving the boundary value problem numerically is more expensive than the analytical approach the use of the 2.5DD model was not considered feasible.

5.3 Stress versus strain-controlled experiments

The characteristic stress-strain curve for stress-controlled fatigue experiments is shown in Figure 5.2 (a). In the first cycle the material is soft, not many dislocations form junctions and the material therefore shows little hardening in the plastic regime. With continued cycling the number of dislocations increases. The dislocations form junctions and hinder the movement of each other. This hardening leads to an increase in the plastic slope with continued cycling. Furthermore, since the maximal admissible stress within each cycle is prescribed, the plastic strain is decreasing in each cycle.

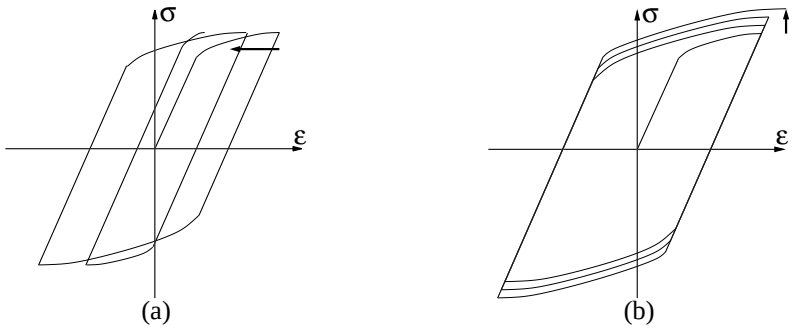

Figure 5.2: Hysteresis loop for stress-controlled (a) and plastic strain-controlled (b) experiments.

Strain-controlled experiments are more common. Here, the plastic strain in each cycle is prescribed. During these experiments, stress the total strain are measured, which are then used to control the plastic strain. The hardening also increases with this loading condition from one cycle to the next, but since the plastic strain has to reach a constant value in each cycle, the maximum applied stress reached per cycle increases. After thousands of cycles the dislocation density saturates. Therefore, the hardening saturates and the maximum applied stress reaches a saturation level.

5.4 Results for stress and strain-controlled simulations

First we look at the stress-strain response predicted under stress control as described in chapter 2. In this stress-controlled simulation, the difference between the average displacement of the left-hand with respect to the right-hand grain boundary is used to calculate the strain.

We apply a cyclic stress, as shown in figure 2.1, and evaluate the strain. The result of this stress-controlled simulation is shown in figure 5.3. The difference between the elastic and plastic regime is well defined in the first cycle. The slope in the plastic regime is high since the grain is constrained by the surrounding elastic half-space. The fact that the attained strain reduces with increased cycling agrees with the expectation in figure 5.3.

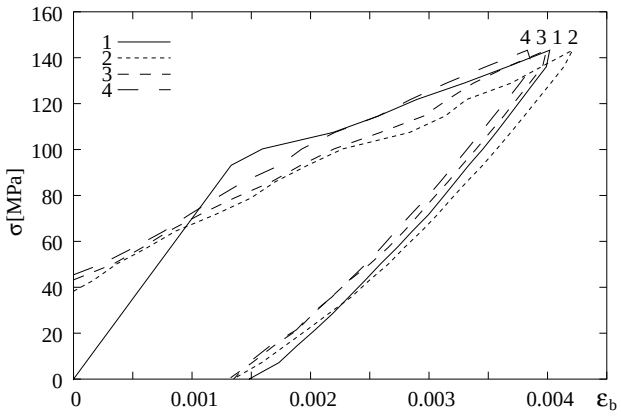

Figure 5.3: Stress-strain curve for stress-controlled simulations, for cycles 1 to 4.

We suspect that the reason for the first cycle moving to a higher strain, rather than to a lower strain, lies in the chaotic nature of dislocation movement, as shown by Deshpande et al. [38].

To simulate strain-controlled fatigue in a polycrystalline material, we model a grain inside a uniform isotropic continuum. To that end, we perform simulations for a $2\mu\mathrm{m} \times 2\mu\mathrm{m}$ grain at the free surface which is embedded in a $24\mu\mathrm{m} \times 13\mu\mathrm{m}$ computational cell, see figure 5.4.

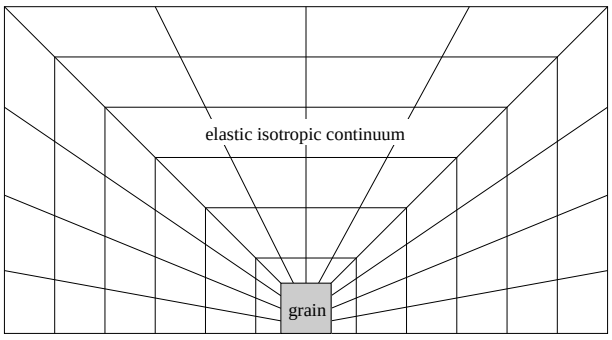

Figure 5.4: Computational cell for the strain-controlled simulations.

To compare the stress and strain-controlled results, we measure the displacements, which are used to calculate the strain, at the grain boundaries. For this simulation the dis-

placements are controlled at the boundary of the computational cell. In figure 5.5 the plastic regime is clearly distinguishable from the elastic regime in the hysteresis loop. Moreover, the stress-strain response at the grain boundaries is soft. However, the hysteresis loop shows stress-controlled characteristics, i.e. the attained stress is roughly constant during the simulation and the maximal attained strain is decreasing due to hardening. Therefore, stress and strain-controlled simulations lead to the same material stress-strain response for a grain inside a relatively large elastic continuum.

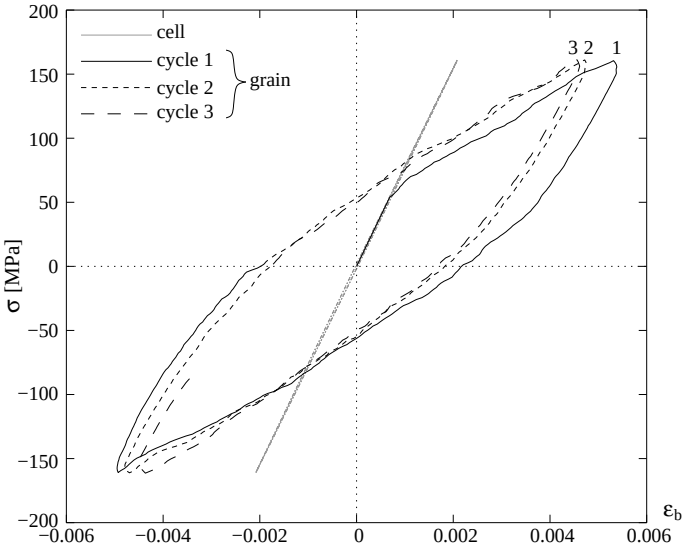

Figure 5.5: Stress-strain hysteresis loop measured at the grain boundary for 3 cycles for strain-controlled simulations in a $2\mu\mathrm{m} \times 2\mu\mathrm{m}$ grain. The stress-strain curve of the computational cell (figure 5.6) is shown as reference.

In terms of the overall strain ε, based on the displacements at the boundary of the computational cell, the plastic region is not well defined and the stress-strain response is much harder than the one at the grain boundary, as shown in figure 5.6 (a). The irreversibility on this macroscopic cell is small. However, in fatigue only a small irreversibility is necessary to cause failure.

We zoom to the upper right-hand corner of the hysteresis loop to find the evolution of the maximum stress over time. As shown in figure 5.6 (b), the maximum stress rises. However, this evolution is not monotonic, which is again attributed to the chaotic nature of dislocations.

Let us look at the reason for the grain having almost no influence on the stress-strain behavior for strain-controlled simulations, as shown in figure 5.6 (a). For the stress and strain-controlled simulations the displacement, which is used to calculate the strain, is mea-

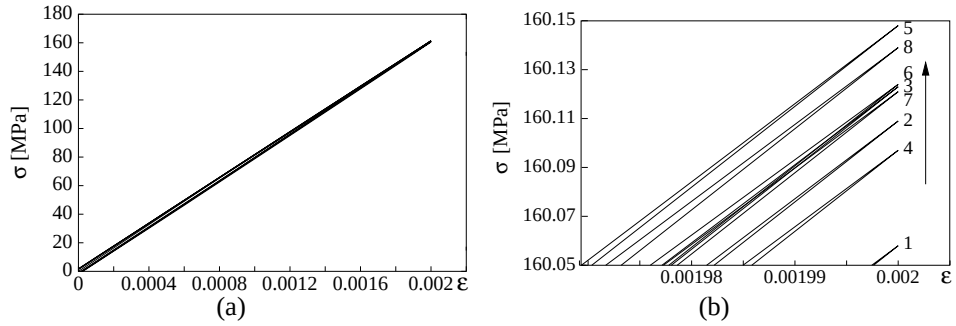

Figure 5.6: Macroscopic stress-strain curve for strain-controlled simulations (a). Zoom of the maximal strain region (b).

sured at different sites. For stress-controlled simulations the displacements are measured along the grain boundary, as mentioned above. However, for the strain-controlled simulations the displacements and stresses are measured at the boundary of the computational cell. Moreover, the grain is small compared to the computational cell, as shown in figure 5.4. The size of the computational cell is chosen such that the elastic fields due to the grain are negligible at the boundaries of the computational cell according to St. Venant's principle; the proportion of the grain to the computational cell is $1 : 10$.

In this work, we try to model a plastic grain inside a macroscopic polycrystalline material. Therefore, the grain is subjected to remote strain-controlled boundary conditions. In the simulation the influence of the plastic grain inside the elastic continuum is small on the macroscopic material, as it is shown in figure 5.6 (a). Moreover, the influence of the plasticity in the grain on the elastic fields at the boundary is necessarily small in this configuration.

5.5 Influence of grain size and shape on the stress-strain curve

We return to the stress-controlled simulations to study the stress-strain response for various grain sizes and grain shapes. We chose the stress-controlled model over the strain-controlled because of its simplicity.

The Orowan equation is given by

$$\dot{\varepsilon} = b\rho_{\mathrm{disl}} v_{\mathrm{disl}},$$

where ρ_{disl} is the mobile dislocation density and v_{disl} is the average dislocation velocity. Time-integration leads to

$$\varepsilon = b\rho_{\mathrm{disl}} s_{\mathrm{disl}}, \tag{5.1}$$

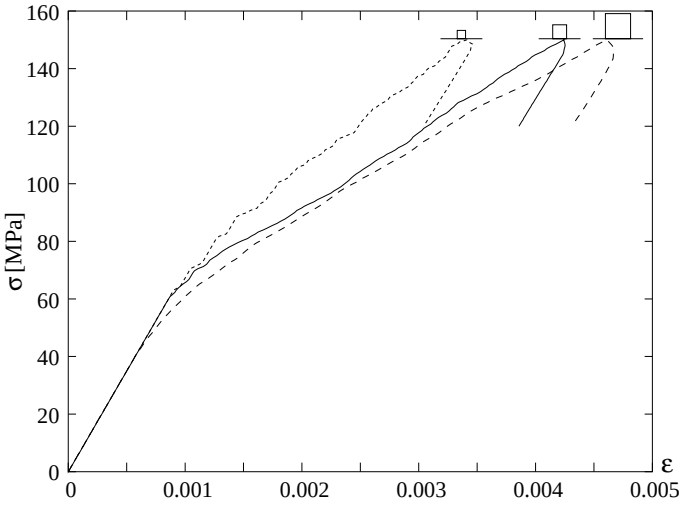

Figure 5.7: Stress-strain curve for a $1\mu\mathrm{m} \times 1\mu\mathrm{m}$, $2\mu\mathrm{m} \times 2\mu\mathrm{m}$ and $4\mu\mathrm{m} \times 4\mu\mathrm{m}$ grain surrounded by an elastic continuum.

where s_{disl} is the average the dislocations have traveled. The average path of a dislocation decreases when the grain size decreases due to the impenetrable grain boundary. According to equation (5.1), therefore, the dislocation density increases to accompany the same plastic strain. Furthermore, because of the higher dislocation density, hardening is stronger for small grains, as shown in figure 5.7 for 1×1, 2×2 and $4 \times 4\mu\mathrm{m}^2$ grains. The density of obstacles and dislocation sources is the same in all grains. Small grains are harder than large grains, which is called the Hall-Petch effect. Furthermore, large grains have a smoother stress-strain curve than small grains, as shown in figure 5.7. In larger grains there are more discrete dislocations, which average out the discrete effects like nucleation, pinning, annihilating or dislocations moving out at the free surface. For much larger grains an even smoother and softer curve than the curve for the $4\mu\mathrm{m} \times 4\mu\mathrm{m}$ grain is expected, which is likely to approach an elastic-perfect plastic stress-strain curve for an infinitely large grain.

Figure 5.8 reveals an additional reason for the hardness of small grains during stress-controlled simulations. The figure shows the displacement parallel to the free surface normalized by the grain width. The displacements are small far inside the elastic continuum, but along the grain boundaries the influence of the plastic grain increases because the grain is softer. The region along the grain boundary where the elastic surrounding decreases the displacement can be taken to have a constant size independent of the grain size, as can be seen by comparison of the $1\mu\mathrm{m} \times 1\mu\mathrm{m}$ and $2\mu\mathrm{m} \times 2\mu\mathrm{m}$ grain. Therefore, the area fraction where the displacements are mainly influenced by the hard surrounding is increasing for

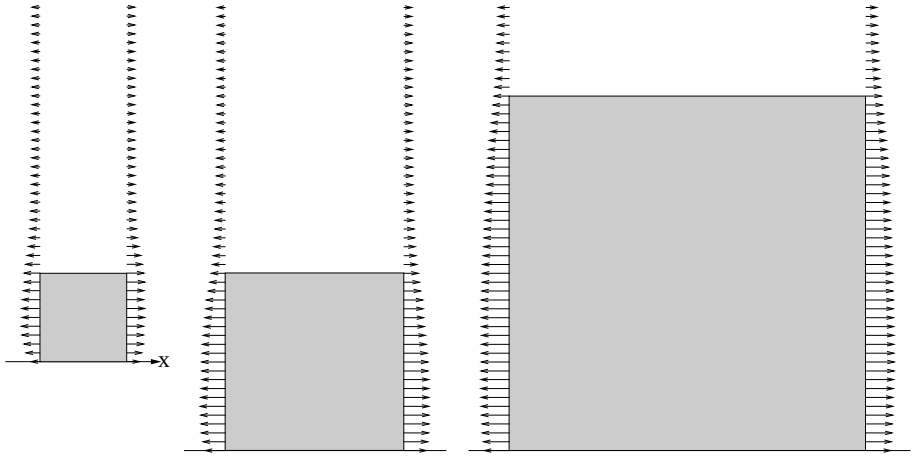

Figure 5.8: Displacement in the x-direction normalized by the width of the grain for a $1\mu\mathrm{m} \times 1\mu\mathrm{m}$, $2\mu\mathrm{m} \times 2\mu\mathrm{m}$ and $4\mu\mathrm{m} \times 4\mu\mathrm{m}$ grain surrounded by an elastic continuum at the peak stress of the first cycle, magnified by factor 100.

smaller grains.

The shape of the grain is square in most simulations presented in this thesis to allow dislocations to form structures. To study the influence of the grain shape on the stress-strain response, results for $2\mu\mathrm{m} \times 1\mu\mathrm{m}$, $1\mu\mathrm{m} \times 2\mu\mathrm{m}$ and $\sqrt{2}\mu\mathrm{m} \times \sqrt{2}\mu\mathrm{m}$ grains are shown in figure 5.9. The density of obstacles and dislocation sources is the same in all grains. The square grain is softest because the maximum slip plane length, i.e. the maximum distance a dislocation can travel, is longer. This grain, therefore, exhibits the least hardening due to grain boundaries. The tall and the wide grain have the same maximum slip plane length. However, the taller grain is softer, as explained above and by figure 5.8. In this grain, the area fraction of the grain boundary is smaller in which displacements are influenced by the elastic – and therefore hard – continuum surrounding. Therefore, the tall grain has a s softer stress-strain response than the wide grain.

Summarizing this chapter, the difference between the stress and strain-controlled experiments is revealed in the evolution of the stress-strain hysteresis loop. For stress-controlled simulations the grain size and shape influence the stress-strain response: smaller and wider grains are harder. The hysteresis loop measured at the grain boundaries for the strain-controlled simulations is similar to the one of the stress-controlled simulation. For strain-controlled simulations the computational cell is sufficiently large that the plasticity inside the grain does not influence the elastic fields at the boundaries of the computational cell. Furthermore, with this approach it is possible to simulate a grain of arbitrary shape inside a uniform continuum that represents a polycrystalline material. The strain-controlled simu-

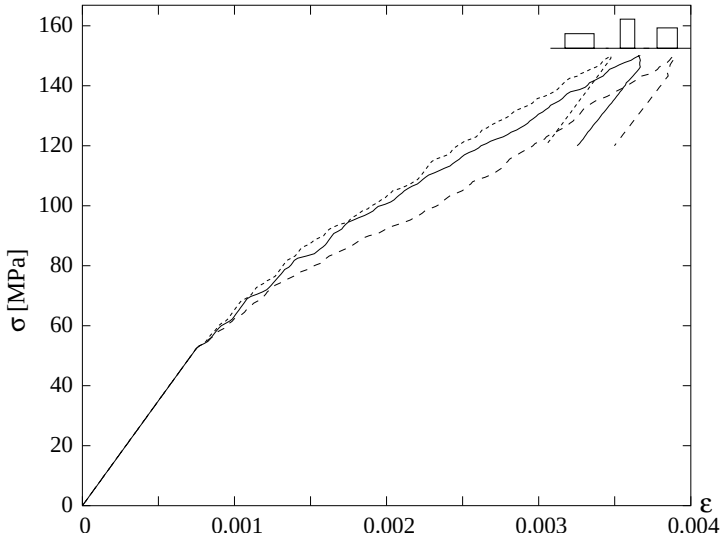

Figure 5.9: Stress-strain curves for grains with the same area but different shapes, $2\mu\mathrm{m} \times 1\mu\mathrm{m}$, $1\mu\mathrm{m} \times 2\mu\mathrm{m}$ and $\sqrt{2}\mu\mathrm{m} \times \sqrt{2}\mu\mathrm{m}$, for stress-controlled simulations.

lations are, therefore, a step into the direction of the 'QuoVaDis' model, which is described next in chapter 6.